Thin-Walled Structures 183 (2023) 110340

Contents lists available at ScienceDirect

Thin-Walled Structures

journal homepage: www.elsevier.com/locate/tws

Full length article

Numerical prediction and experimental analysis of the buckling loads of SMPC cylindrical shells under axial compression

Hanxing Zhao [a], Xin Lan [a,*], Liwu Liu [b], Yanju Liu [b], Jinsong Leng [a,*]

[a] Centre of Composite Materials and Structures, Harbin Institute of Technology (HIT), Harbin 150080, People's Republic of China
[b] Department of Astronautical Science and Mechanics, Harbin Institute of Technology (HIT), Harbin 150001, People's Republic of China

ARTICLE INFO

Keywords:
SMPC
Cylindrical shell
KDF
Buckling load
Repeatability

ABSTRACT

The axial compressive buckling loads of shape memory polymer composite (SMPC) cylindrical shells are very sensitive to geometric imperfections and temperatures, but few studies have been conducted on this phenomenon. In this study, the buckling loads and geometric imperfection sensitivities of SMPC cylindrical shells at different temperatures are determined by means of numerical simulations and experimental analyses. The single perturbation displacement imperfection (SPDI), multiple perturbation displacement imperfection (MPDI) and linear buckling mode imperfection (LBMI) techniques are used to simulate the initial geometric imperfections and calculate the corresponding buckling loads and knock-down factors (KDFs) of SMPC cylindrical shells at different temperatures. In the experimental part, the $[0/90/\pm45]_s$ SMPC cylindrical shells are manufactured through the autoclave molding process. The load-bearing capacities at different temperatures are tested and compared with the numerical results. The results demonstrate that the buckling loads of the SMPC cylindrical shell obtained by numerical techniques are sensitive to temperature, while the KDFs are insensitive to temperature. Meanwhile, results indicate that brittle fracture is the main failure mode instead of buckling at low temperature, so there is a risk when using any numerical technique to design SMPC cylindrical shells in low-temperature region. At high temperatures, the SPDI method overestimates the KDFs, while the KDFs calculated by the MPDI and LBMI techniques are in good agreement with the experimental results. However, only the LBMI method can distinguish the influence of temperature on the post-buckling patterns, and the corresponding post-buckling pattern is more consistent with the experiment. In addition, the shape-recovery properties and repeatability of the SMPC cylindrical shells are good.

1. Introduction

Fiber-reinforced polymer composites (FRPCs) have the advantages of high specific modulus, high specific strength, good fatigue resistance, and they are easily formed into desired shapes, which make them increasingly irreplaceable in aerospace applications [1,2]. Compared with traditional polymers, shape memory polymers (SMPs) are a new type of smart material that can change shape with changes in external stimuli without external forces and have received increasing attention [3,4]. At present, the applications of SMPs and shape memory polymer composites (SMPCs) in the aerospace field mainly include space deployable hinges, trusses and antennas [5–7]. Most of these structures are SMPC plates; SMPC cylindrical shells, which are excellent load-bearing structures, have not been widely used [8,9]. The reason for their lack of use is that the structure and external load conditions of the SMPC cylindrical shells are relatively more complex than those of the SMPC plates, which makes it difficult to analyze the load-bearing capacity (the buckling load). In addition, as a temperature-sensitive material, the mechanical properties of SMPCs will change dramatically with temperature, so the buckling behaviors of SMPC cylindrical shells are quite different from those of general FRPC cylindrical shells.

The prediction of the axial buckling load of cylindrical shell structures has been a popular topic of research. However, it is found that the theoretical buckling loads of cylindrical shells are always quite different from the experimental results due to the geometric, loading and material imperfections [10–12]. These inevitable imperfections are caused during manufacturing or experimental processes, where geometric imperfections are the most common and unavoidable [13]. The axial buckling load of a cylindrical shell is very sensitive to temperature. Thus, the practical buckling loads of cylindrical shells are always much lower than the theoretical values. The load-bearing capacities are insufficient if the cylindrical shells are designed according to the theoretical calculation results, which leads to premature destruction of the structures. Therefore, the concept of the knock-down factor (KDF) [14,15] is proposed to quantify such errors.

* Corresponding authors.
E-mail addresses: lanxin@hit.edu.cn (X. Lan), lengjs@hit.edu.cn (J. Leng).

https://doi.org/10.1016/j.tws.2022.110340
Received 7 May 2022; Received in revised form 10 October 2022; Accepted 2 November 2022
Available online xxxx
0263-8231/

The KDF is the ratio of the maximum axial load-bearing capacity of a cylindrical shell in practical applications to its theoretical critical buckling load. The value of the KDF ranges from 0.2 to 1 for most cylindrical shells, depending on the amplitudes of geometric and loading imperfections [13]. As early as the 1960s, the NASA SP-8007 monograph proposed an empirical equation for the KDF based on a large amount of experimental data [16]. Since then, this formula has been widely used to determine the practical buckling loads of cylindrical shell components based only on the dimensional parameters, i.e., $\mathrm{KDF} = 1 - 0.901 \times (1 - e^{-\sqrt{R/t}/16})$. However, the calculation results are always too conservative because the material properties are not considered [17]; thus, cylindrical shells made according to this design criterion will be too thick. The excessive weight of the structures will affect the payloads of the launch vehicles and aircraft, which is exactly what the aerospace fields should avoid. Therefore, in recent years, the imperfection sensitivities of thin-walled cylindrical shells have been widely studied based on theoretical and finite element analyses, and the main idea is to artificially introduce initial geometric imperfections into a perfect cylindrical shell and then study its stability.

Wang et al. [17,18] introduced the measured geometric imperfections into the numerical model through digital image correlation (DIC) technology. It was found that the measured imperfections could well simulate the initial geometric imperfections of the cylindrical shell, and the numerical results showed good agreement with the experimental results. However, this technique cannot be performed in the preliminary design stage. Sosa et al. [19] used the linear buckling mode imperfection (LBMI) method to investigate the imperfection sensitivities of cylindrical shells. The main idea of this method is introducing the linear buckling mode shape imperfection into the perfect cylindrical shell after being scaled in a certain proportion, which is a commonly used method in simulating the post-buckling behaviors of cylindrical shells. Hühne [20] used the single perturbation load imperfection (SPLI) method to quantify the imperfection sensitivities of cylindrical shells, and he called this dimple-shaped perturbation the “worst”, “realistic” and “stimulating” imperfection. Arbelo and Chen [21–23] modified the SPLI method and proposed multiple perturbation load imperfection (MPLI), worst multiple perturbation load imperfection (WMPLI) and random perturbation load imperfection (RPLI) techniques, which could better predict the practical buckling loads of cylindrical shells because they increased the number of perturbation load imperfections (PLIs) compared with the SPLI method. The dimple-shaped imperfections are directly introduced into the side of the cylindrical shells in the SPLI, MPLI, WMPLI and RPLI methods, and with the increase in the number of PLIs, the buckling loads will gradually decrease until convergence, so that the KDF can finally be obtained.

In addition, many numerical methods for calculating the imperfection sensitivity of thin-walled cylindrical structures have been proposed in recent years. The single boundary perturbation imperfection (SBPI) method [24] introduces local boundary perturbations on the top of the shells to induce dimple-shaped imperfections indirectly. In addition to dimple-shaped imperfections, Fathollah et al. [25,26] used cutout (CR) to investigate the buckling loads of composite cylinders. Evkin and Horak et al. [27–30] proposed analytical models to calculate the local buckling load of cylindrical shells, and the different boundary conditions were also considered. Wagner [31] and Hao [32] used the reduced or incomplete reduced stiffness method to investigate the imperfection sensitivity of cylindrical shells. In addition to the numerical and theoretical methods, Chen and Jiao [33–36] also completed plenty of experiments to investigate the buckling behaviors of cylindrical shells.

As mentioned above, there has been much research on the imperfection sensitivities of cylindrical shell structures, while only a few of them are related to FRPC cylindrical shells (they mainly focus on isotropic materials, such as steel). To the best of our knowledge, few studies have been conducted on the geometric imperfection sensitivity of SMPC cylindrical shells under axial compression. In this study, the influence of temperature on the buckling behavior of SMPC cylindrical shells is studied in a novel way. The temperature is divided into a low-temperature region and a high-temperature region. The compressive failure mode of SMPC cylindrical shells in the low-temperature region is dominated by brittle fracture, while that in the high-temperature region is dominated by buckling. The numerical and experimental methods are combined to study the buckling behaviors of SMPC cylindrical shells. In the numerical simulations, single perturbation displacement imperfection (SPDI), multiple perturbation displacement imperfection (MPDI) and LBMI techniques are used to simulate the initial geometric imperfections and calculate the buckling loads and KDFs of SMPC cylindrical shells at different temperatures. In the experimental part, the $[0/90/\pm45]_s$ SMPC cylindrical shell is manufactured through an autoclave molding process. The load-bearing capacities at different temperatures are tested and compared with the numerical results. In addition, we propose that the SMPC cylindrical shell can be applied to the auxiliary vibration reduction structure of the space pyrotechnic releasing mechanism and performed repeated experiments on the shape-recovery process of a buckled SMPC cylindrical shell. In this study, the effects of temperature on buckling loads, KDFs and post-buckling patterns of SMPC cylindrical shells are investigated by numerical and experimental analyses, which can play a guiding role in the preliminary design of SMPC cylindrical shells.

2. Numerical simulations

The single perturbation displacement imperfection (SPDI), multiple perturbation displacement imperfection (MPDI) and linear buckling mode imperfection (LBMI) techniques are introduced in this study to verify the geometric imperfection sensitivities of SMPC cylindrical shells at different temperatures and obtain the corresponding buckling loads, KDFs and post-buckling patterns. In this section, these numerical methods are investigated.

2.1. Finite element model preparation

Before performing the subsequent numerical simulations and experimental analysis of the buckling loads and geometrical imperfection sensitivities of SMPC cylindrical shells at different temperatures, some key parameters, such as the overall size, fiber stacking configurations and mesh size, should be first determined by linear buckling analysis. In this section, the commercial software Abaqus 6.14 is used to determine the critical buckling loads of perfect cylindrical shells under axial compression. The boundary conditions are assumed to be clamped (the same as in the subsequent experiments), and all the degrees of freedom of the top and bottom edges of the shell are kinematically coupled by two reference points. All six degrees of freedom of the bottom edge are constrained. For the top edge, all five degrees of freedom except for the axial motion are constrained, and a compressive concentrated force in the axial direction is applied at the reference point. The material properties of SMPC at different temperatures are shown in Table 1, and the detailed testing procedures are provided in the Supplemental file. G_{13} and G_{23} are assumed to be approximately equal to G_{12}, and the thickness of a single lamina is 0.15 mm. The linear perturbation-buckling analysis step is used to determine the critical buckling load, and the subspace algorithm is adopted to guarantee the accuracy. The element type is S4R, and the critical buckling load can be calculated by multiplying the eigenvalue by the previously applied concentrated force.

To determine the best fiber stacking configuration, in this section, eight kinds of typical fiber stacking configurations $[0]_8$, $[\pm45]_4$, $[\pm45]_{2s}$, $[0/90]_4$, $[0/90]_{2s}$, $[0/90/\pm45]_s$, $[0/90/\pm60]_s$, and $[90]_8$ are compared. In addition, a dimensional parameter of the cylindrical shell $Z = 0.6L^2/Rt$ is considered to investigate the influences of the length-to-radius ratio and length-to-thickness ratio on the critical buckling loads, where the radius R and thickness t of the cylindrical shell are 20 mm and 1.2 mm,

Table 1
The lamina properties of SMPC at different temperatures.

	Temperature (°C)	25	40	60	80	100
Carbon fiber reinforced SMPC	E_{11} (MPa)	40 653	34 053	25 559	19 558	16 676
	E_{22} (MPa)	12 491	10 460	3732	17.3	9.04
	υ_{21}	0.29	0.77	0.63	0.44	0.41
	G_{12} (MPa)	814	574	37.4	27.2	21.2

respectively. The overall length L is chosen to be 20 mm, 40 mm, 60 mm, 80 mm, 100 mm, 120 mm and 200 mm in this section; the corresponding Z can be calculated as 10, 40, 90, 160, 250, 360 and 1000, respectively. It should be noted that the calculation accuracy will be improved with the decrease of the mesh size, but the calculation cost will simultaneously be greatly increased. Therefore, the proper mesh size should be determined first. Table 2 shows the critical buckling loads corresponding to different mesh sizes (numbers of meshes) for the $[0/90/\pm45]_s$ SMPC cylindrical shell with the dimensional parameter $Z = 10$ at 25 °C. The critical buckling loads decrease gradually with the increase in the number of meshes and finally tend to converge. In this study, considering the accuracy and efficiency of the FEA simultaneously, the mesh size is chosen to be the same as Z10-6 in Table 2 for all the SMPC cylindrical shells. With the increase in Z, the size of the mesh will not change, and only the number of meshes will increase.

Fig. 1 shows that the critical buckling loads are greatly influenced by the fiber stacking configurations, e.g., the $[0/90/\pm\theta]_s$ cylindrical shell has the largest critical buckling load, while the $[90]_8$ cylindrical shell has the lowest critical buckling load. In addition, the critical buckling loads of symmetrical laminated cylindrical shells are slightly larger than those of anti-symmetric laminated cylindrical shells with the same ply angle, but the differences are so small that they can be neglected. In the meantime, with the increase in the dimensional parameter Z, the critical buckling loads will decrease rapidly for all cylindrical shells until $Z > 100$, and then the critical buckling loads will gradually converge to constant values.

It can also be seen from Fig. 1 that the levels of Z-sensitivity of cylindrical shells with different fiber stacking configurations are also different. As Z increases from 20 to 1000, the critical buckling loads of the $[0]_8$, $[0/90]_{2s}$ and $[0/90]_4$ cylindrical shells have the largest reductions, up to 46.5%, 40.6% and 35.5%, respectively; the declining magnitudes of the $[90]_8$, $[\pm45]_{2s}$ and $[\pm45]_4$ cylindrical shells are not that dramatic, which are approximately 25% for all three cases; the critical buckling loads of the $[0/90/\pm45]_s$ and $[0/90/\pm30]_s$ cylindrical shells have the lowest sensitivity to Z (as Z increases from 20 to 100, the critical buckling loads only decrease by 12.7% and 14.3%, respectively). Fig. A.1 shows the first-order linear buckling mode shapes of SMPC cylindrical shells with different fiber stacking configurations and Z at 25 °C. It can be seen that the buckling wavenumber in the axial direction of the $[0/90/\pm\theta]_s$ cylindrical shells is independent of Z, while it will increase with the increase in Z for other fiber stacking configurations. The above two points indicate that the critical buckling loads of $[0/90/\pm\theta]_s$ cylindrical shells are not sensitive to the dimensions.

Therefore, the $[0/90/\pm45]_s$ cylindrical shells are used for the subsequent numerical and experimental investigations when simultaneously considering the load carrying abilities and the degrees of dimensional sensitivities. In addition, Z is chosen to be 90 in the following sections (the overall length is 60 mm, the radius is 20 mm and the thickness is 1.2 mm).

2.2. SPDI and MPDI techniques

The basic ideas of the SPDI and MPDI techniques are shown in Fig. 2, and there are two steps: (1) The perturbation displacement imperfections (PDIs) are applied to the outer side of the cylindrical shell, and the corresponding dimple-shaped deformations are obtained by nonlinear static analysis. Then, the imperfection is introduced into a perfect SMPC cylindrical shell by modifying the coordinates of nodes using the .inp file of Abaqus. (2) The Nonlinear Riks Method is used for the following nonlinear buckling (post-buckling) analysis, and the load-carrying capacity (buckling loads) of the imperfect cylindrical shell can be obtained. The lower bound of the buckling loads of SMPC cylindrical shells can be determined by changing the amplitudes and positions of the PDIs, and thus, the corresponding KDFs can be obtained. It should be noted that the flexural stiffness of SMPC will decrease drastically with increasing temperature, and different dimple-shaped deformations will be caused by the same perturbation load at different temperatures. Therefore, the perturbation displacement imperfection is utilized in this study instead of the perturbation load imperfection.

Fig. 3 shows the distribution of the PDIs of the SPDI and MPDI techniques. The most common form of PDIs is used in this study,

Table 2
The mesh convergence study of $[0/90/\pm45]_s$ SMPC cylindrical shell with the dimensional parameter Z = 10 at 25 ° C.

Serial number	Number of meshes (elements around circumference and axial)	The buckling loads (kN)
Z10–1	10 × 5	101.75
Z10–2	20 × 10	95.06
Z10–3	40 × 20	90.80
Z10–4	60 × 30	87.45
Z10–5	80 × 40	86.32
Z10–6	100 × 50	85.80
Z10–7	120 × 60	85.52

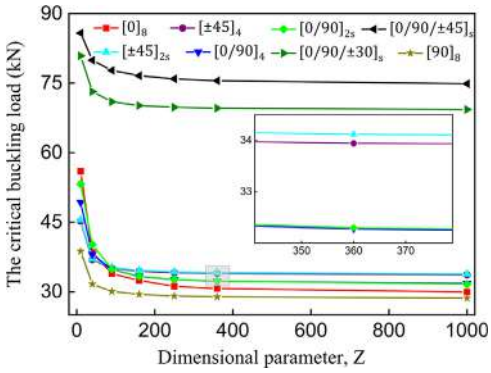

Fig. 1. The critical buckling loads as a function of the Z of the cylindrical shell at 25 °C (the 1st buckling mode).

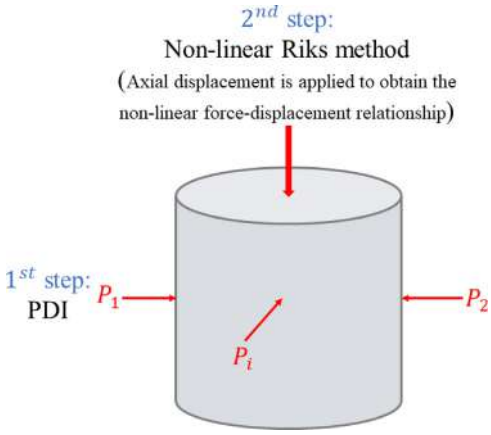

Fig. 2. The basic ideas of the SPDI and MPDI techniques.

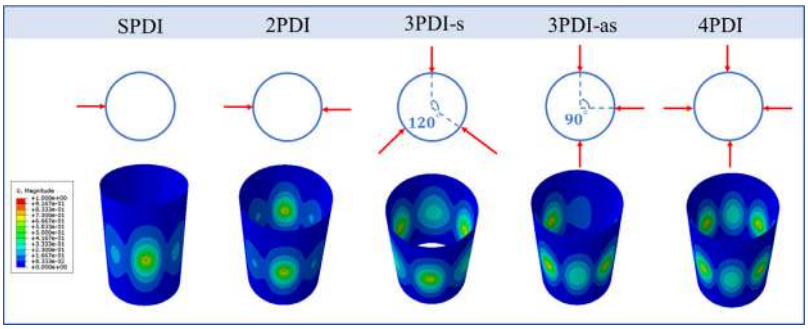

Fig. 3. Diagram of the distribution of perturbation displacements of SPDI and MPDI techniques, and the corresponding initial imperfections patterns of $[0/90/\pm45]_s$ SMPC cylindrical shells at 25 °C (the amplitude of perturbation displacements is 1 mm, and the deformation scale factor is 1).

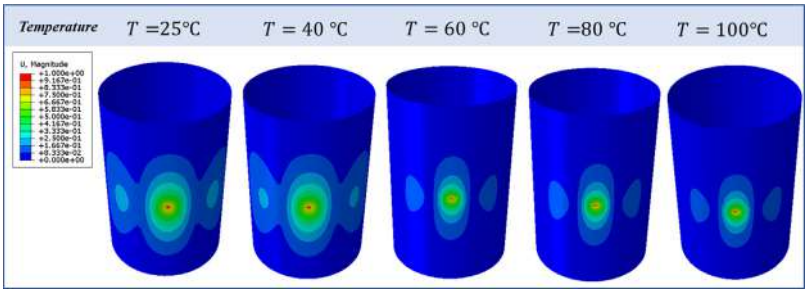

Fig. 4. The initial imperfection patterns of $[0/90/\pm45]_s$ SMPC cylindrical shells obtained by SPDI (the amplitude of perturbation displacements is 1 mm, and the deformation scale factor is 1).

i.e., the perturbation displacements are distributed at the middle height of the cylindrical shell with the same amplitude. In this section, 1, 2, 3, and 4 PDIs are designed at the middle of the outer side of the cylindrical shell. The 3 PDIs case can be divided into symmetrical and asymmetrical cases, so there are a total of 5 cases in this section. The corresponding initial imperfection patterns (the initial imperfect shape in the 2nd step of Fig. 2) of $[0/90/\pm45]_s$ SMPC cylindrical shells at 25 °C can also be seen in Fig. 3, where the amplitude of perturbation displacements is 1 mm. It can be seen that the area of the initial dimple-shaped imperfections of the cylindrical shell increases with the increasing number of PDIs. In addition, SMPC is a kind of thermosensitive material, and the effect of temperature on the initial imperfection patterns caused by PDIs should also be investigated. Fig. 4 shows the initial imperfection patterns of $[0/90/\pm45]_s$ SMPC cylindrical shells obtained by the SPDI method at different temperatures, where the amplitude of perturbation displacements is also kept at 1 mm. It can be concluded that the shape of the initial imperfection is independent of temperature, and only the area is slightly reduced with increasing temperature.

2.3. LBMI method

The geometrical imperfections introduced by the SPDI and MPDI techniques are not localized in the axial direction, and the shapes of SPDI and MPDI are independent of temperature. To overcome the above two shortcomings, the LBMI method is also introduced in this study to calculate the buckling loads and KDFs of SMPC cylindrical shells at different temperatures. The procedure of the LBMI method is as follows: the linear buckling mode of the cylindrical shell is multiplied by a scaling factor δ as the initial imperfection, and the subsequent steps are all the same with the SPDI and MPDI techniques. Although the linear buckling eigenmode shapes are quite different with different modes, Fathollah and Milad [10] found that the KDF is only dependent on the scaling factor δ but not on the modes. Therefore, to ensure the consistency of the result, the 1st linear buckling eigenmode shape is selected in this study as the LBMI. Fig. 5 shows the 1st linear buckling eigenmode shapes and the corresponding critical buckling loads of $[0/90/\pm45]_s$ SMPC cylindrical shells at different temperatures. As the temperature increases from 25 °C to 100 °C, the critical buckling loads of the SMPC cylindrical shell will decrease rapidly, and the decrease range will exceed 96%. Notably, the 1st linear buckling eigenmode shapes in the high temperature range (60 °C, 80 °C and 100 °C) and low temperature range (25 °C and 40 °C) are quite different. As shown in Table 1, the ratio of the longitudinal modulus to the transverse modulus of SMPC (E_{11}/E_{22}) is 3.25 at 25 °C, while it will increase to 1845 as the temperature increases to 100 °C. The high degree of anisotropy may result in distorted buckling modes in the high-temperature region (the reason for this phenomenon is beyond the scope of this study).

Compared with SPDI and MPDI, the LBMI will include the initial geometric imperfections along the axial direction of the cylindrical shell. In addition, the shapes of LBMIs are closely related to temperature, which is more consistent with the inherent properties of SMPC materials.

3. Experimental studies

3.1. Specimen preparation

To ensure the quality of the specimens, carbon fiber-reinforced SMPC prepreg tapes were used as raw materials instead of carbon fiber and liquid shape memory epoxy resin. The technology of two-step automated tape laying was applied to manufacture the prepreg tapes, and the detailed preparation steps are shown in Section S1, Supplemental files. The resin was shape memory epoxy resin with a glass transition temperature of 100 °C prepared by Leng's group [37], and the fiber was Toray T300s 12K carbon fiber (Toray Industries Inc., Tokyo, Japan). The material properties of both cured resin and fiber are shown in Table S1, Supplemental files. The specimens were prepared by the hand lay-up process assisted by the autoclave. The fiber stacking configuration of all the specimens is the same as that of the above numerical analyses, i.e., $[0/90/\pm45]_s$.

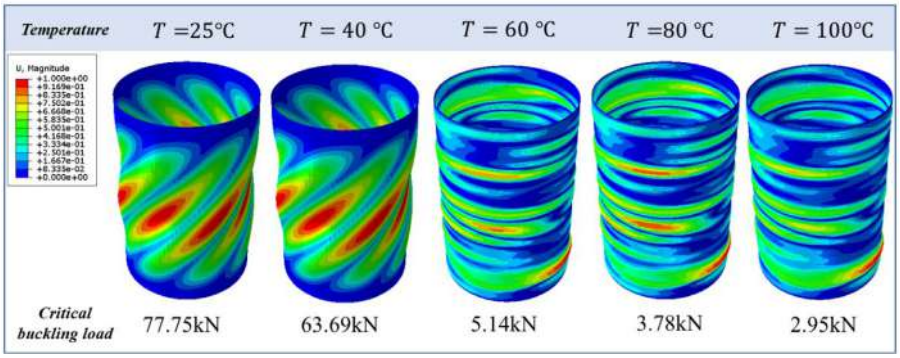

Fig. 5. The 1st linear buckling eigenmode shapes and the corresponding critical buckling loads of $[0/90/\pm45]_s$ SMPC cylindrical shells at different temperatures (Z = 90, the deformation scale factor = 1).

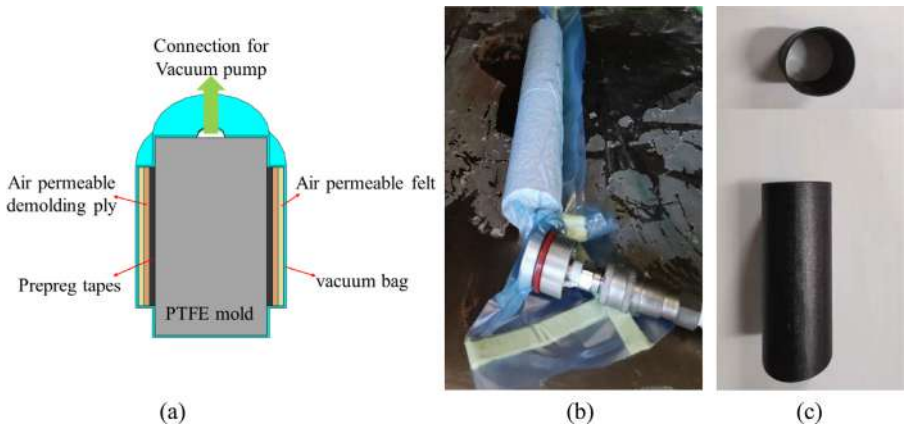

Fig. 6. The fabrication of SMPC cylindrical shells. (a) sketch of the cylindrical mold, (b) curing process of the SMPC cylindrical shell, and (c) SMPC cylindrical shell.

3.1.1. Specimen preparation of SMPC cylindrical shells

First, the prepreg tape was cut into rectangular shapes according to the dimension parameters of the cylindrical shell, where there were 4 layers of 0° prepreg tape and 4 layers of 45° prepreg tape. The prepreg tape was laid layer by layer with a fiber stacking configuration of $[0/90/\pm45]_s$ on a cylindrical mold after softening by a heat gun. The diameter of the cylindrical mold was 40 mm, and the length was 100 mm. To facilitate demolding, the raw material of this mold was PTFE. To ensure that air was completely removed and wrinkles on prepreg tapes were eliminated during the following vacuuming process, a layer of air-permeable demolding ply and a layer of felt must be wrapped around the prepreg. Finally, the vacuum bag was wrapped, as shown in Fig. 6(a), and the whole specimen was cured by an autoclave (Dalian Yingtian Composite Material Co., LTD, China), as shown in Fig. 6(b). The curing process was set as follows: curing at 80 °C for 3 h, then curing at 100 °C for 3 h and finally curing at 150 °C for 5 h, with a compressive pressure of 0.1 MPa and a vacuum of 0.001 MPa.

3.1.2. Specimen preparation of SMPC plates

To better understand the thermomechanical behaviors of SMPCs with the same fiber stacking configuration, DMA experiments were needed, so SMPC plates were also prepared. First, the prepreg tapes were cut into a rectangular shape with dimensions of 200 mm × 200 mm, where there were 4 layers of 0° prepreg tape and 4 layers of 45° prepreg tape. These 8 layers of prepreg tape were then laid layer by layer with a fiber stacking configuration of $[0/90/\pm45]_s$ between two peel ply-covered rectangular metal molds. The combined molds were subsequently wrapped with a layer of felt, and finally, a vacuum bag was wrapped and vacuumized, with a vacuum of 0.001 MPa, as shown in Fig. 7(a). The subsequent curing process was the same as that of SMPC cylindrical shells.

3.2. DMA tests of the SMPC sheets

The dynamic mechanical properties of SMPC were determined by DMA with the three-point bending mode. All the specimens were cut by a water jet cutting machine (Nanjing Bitong Technology Co., LTD, China) from one large SMPC sheet, as shown in Fig. 7(b), and the average thickness of the SMPC specimens was measured to be 1.5 mm. Therefore, according to the ASTM D5023-15 Standard Test Method, the dimensions of the specimen were 44 mm × 6 mm, and the support span was 22 mm to ensure that the span-to-depth ratio was between 14 and 20. The depth and width of the specimen were measured and recorded at its center, and the specimen was then centered on the supports. During the DMA test, the frequency mode was set as multifrequency with a frequency of 1 Hz, the heating rate was 2 °C/min, and the final temperature was 120 °C. The storage modulus and loss factor (Tan Delta) curves with temperature were output by software. Tan Delta is the loss factor, which is equal to the ratio of the loss modulus and storage modulus.

In the meantime, the DMA test of pure SMP specimens was also conducted, and the results were compared with those of SMPC, which are shown in Fig. 8. The storage moduli of both SMP and SMPC decrease with increasing temperature and eventually stabilize at low values. At the same temperature, the modulus of SMPC is much higher than that of SMP, indicating that the introduction of carbon fibers has greatly improved the load-carrying capacity of the resin matrix. It is worth noting that the temperature corresponding to the peak of the Tan Delta-temperature curve is generally used to describe the glass transition temperature (T_g) of SMP and SMPC. As shown in Fig. 8, the T_g of SMP is approximately 100 °C, while that of SMPC is approximately 30°C less. The main reason for this phenomenon is that the thermal conductivity of the carbon fiber is much higher than that of the epoxy

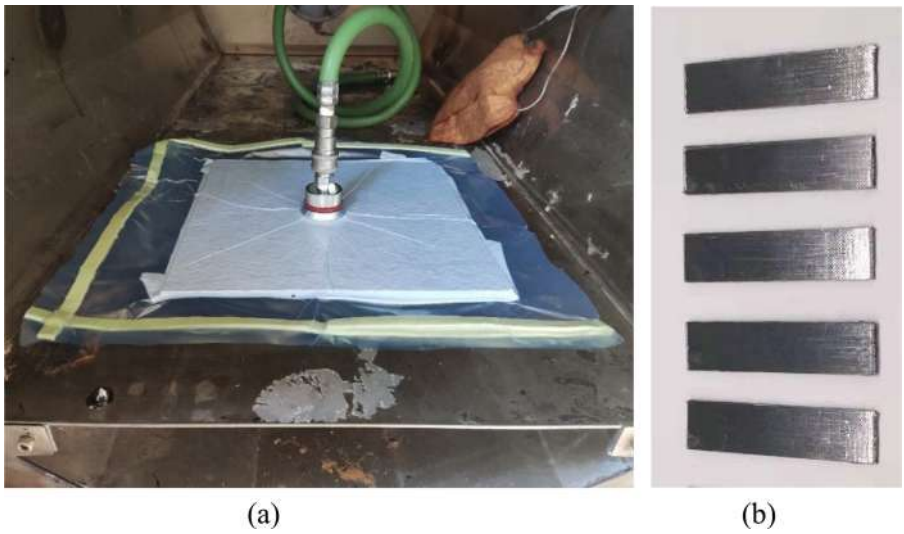

Fig. 7. The fabrication of SMPC sheets. (a) The fabrication process and (b) the SMPC lamellar specimens for DMA tests.

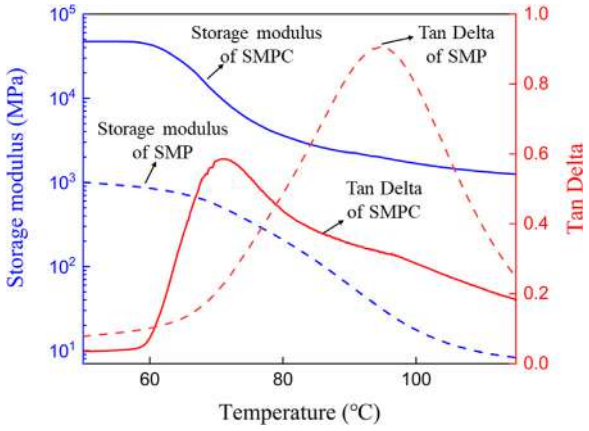

Fig. 8. DMA test results of SMP and SMPC.

resin matrix, so the interior of SMPC will be heated faster at the same external ambient temperature, and the material more easily reaches its T_g. As a result, the introduction of carbon fiber greatly enhances the mechanical properties of shape memory epoxy resin but reduces its glass transition temperature.

3.3. Isothermal buckling tests of SMPC cylindrical shells under axial compression

After the curing process, the cylindrical specimens were demolded as shown in Fig. 6(c). Then, the SMPC cylindrical shell was cut to a length of 70 mm (the free length during the subsequent tests was 60 mm, as shown in Fig. 9). The axial compressive tests were performed by Instron 5569 universal mechanical test instruments to obtain the buckling loads of the SMPC cylindrical shells at 25 °C, 40 °C, 60 °C, 80 °C and 100 °C. It is worth noting that before the experiment, both ends of this SMPC cylindrical shell must be covered with metal clamps to ensure the clamped boundary conditions during the axial compressive test (corresponding to the clamped boundary conditions in the previous theory and FEA), as shown in Fig. 9. After measuring and recording the size of the specimen, it was placed between the compression plate of the test instruments and kept at the preset temperature for 30 min in an oven, as shown in Fig. 10. During the experiment, a 10 N preload was first applied, and then the specimen was compressed at a loading speed of 2 mm/min. A digital signal acquisition system was used to record the force $F(t)$ and displacement $s(t)$ during the compression experiment, and the sampling frequency was 10 Hz. At least five specimens were prepared for each configuration, and the mean values of the test data were calculated to represent the results.

4. Results and discussion

4.1. Parameter study of the SPDI, MPDI and LBMI methods

Taking the $[0/90/\pm45]_s$ SMPC cylindrical shell with the dimensional parameter $Z = 90$ as an example in this section, the effects of the number and amplitude of PDIs on the SPDI and MPDI techniques are studied. In addition, the influence of the scaling factor δ on the LBMI method is also investigated. Besides, since SMPC is highly temperature-sensitive, the effect of temperature on the KDF and post-buckling patterns is taken into consideration.

4.1.1. SPDI

Fig. 11(a) shows the variation of buckling loads of the $[0/90/\pm45]_s$ SMPC cylindrical shell with the perturbation displacement η at 25 °C. As η increases from 0.1 mm to 2 mm, the buckling load decreases rapidly from 77.7 kN to 57 kN and then tends to converge when $\eta = 1$ mm. The main reasons for this phenomenon are as follows: The corresponding imperfection caused by the single perturbation displacement (as shown in the 1st step of Fig. 2) will become larger with the increase in η, and this imperfection will lead to a rapid decrease in the buckling load; when the dimple-shape deformation reaches a certain threshold, only a very small axial compressive load can be borne near this defect, while other parts of the cylinder will bear most of the remaining compressive load. Therefore, the perfect region will occupy the main role in the buckling load, and the imperfection may be irrelevant. In addition, as shown in Fig. 11(c), when η increases from 0.1 mm to 1 mm, the post-buckling patterns are quite different (the end shortening of the cylinder is the same, which is approximately 1.2 mm). The area of the concave region will increase significantly. However, as η continues to grow to 2 mm, the area of the concave region will not change, and only the sunken depth will increase. Therefore, the buckling loads and post-buckling patterns of the cylindrical shell are quite sensitive to η, while once η reaches a certain threshold value, the buckling loads and post-buckling patterns will not continue to change. This threshold value of the $[0/90/\pm45]_s$ SMPC cylindrical shell obtained from the SPDI method is 1 mm, and the corresponding KDF at 25 °C is approximately 0.73.

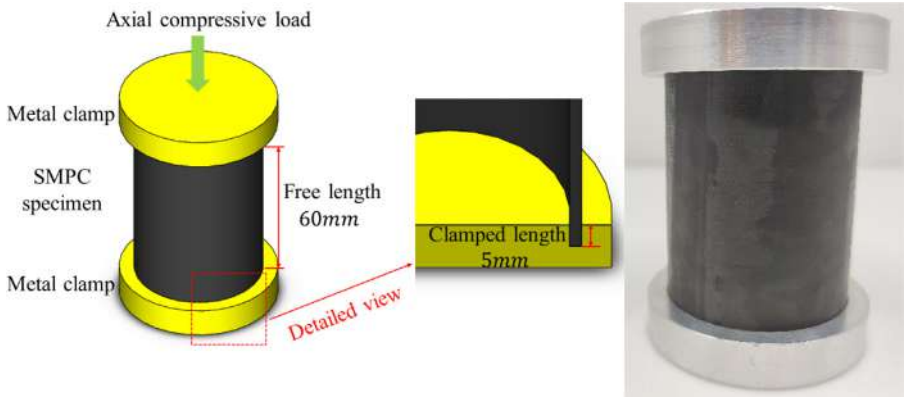

Fig. 9. The tested SMPC cylindrical shells with clamped boundary conditions.

Fig. 10. The axial compressive tests of SMPC cylindrical shells.

Fig. 11(b) shows the variations in buckling loads and KDFs with temperature when η = 1 mm. As the temperature increases from 25 °C to 100 °C, the buckling loads of the $[0/90/\pm45]_s$ SMPC cylindrical shell will decrease from 57 kN to 1.9 kN, which drops by 96.6%, while the KDF only drops from 0.73 to 0.66 (9.5% decrease). It can also be seen from Fig. 11(c) that with increasing temperature (when the temperature is 25 °C and 100 °C), the post buckling patterns are almost the same (the area of the concave region will not increase), so the decrease in KDF is not significant. Therefore, we can conclude that the buckling loads of the SMPC cylindrical shell obtained by the SPDI technique are sensitive to temperature, while the post-buckling patterns and KDFs are insensitive to temperature.

4.1.2. MPDI

Fig. 12 shows variations in KDFs with the amplitudes of perturbations of all four MPDI cases at 25 °C. It can be seen that the KDF will converge when the amplitude of perturbations η is approximately 1 mm, and with the increase in the number of perturbation displacements, the final KDF will become lower. This is because the area of the perfect region of the cylindrical shell will gradually decrease with increasing amplitude and number of perturbation displacements, which will lead to a decrease in KDF. This phenomenon can also be seen in Fig. 13. The area of the concave region increases significantly as the number of perturbation displacements increases, so the KDF decreases simultaneously. It is worth noting that the final KDF of the 3PDI-as case is only approximately 0.6 and is even lower than that of the 4PDI case, which indicates that the increase in the degree of asymmetric distribution of PDIs will lead to a decrease in the KDF. Therefore, the 3PDI-as case is more sufficient to simulate the geometric imperfections of SMPC cylindrical shells. Hereinafter, MPDI will be represented by 3PDI-as (η = 1 mm), and then the influence of temperature on KDFs will be investigated by the MPDI technique.

Table 3
The buckling loads and KDFs of $[0/90/\pm45]_s$ SMPC cylindrical shell under different temperatures by MPDI method.

Temperature (°C)	Buckling load of 3PDI-as (kN)	KDF
25	47.2	0.607
40	38.3	0.602
60	2.92	0.568
80	2.13	0.563
100	1.65	0.56

It worth noting that the initial imperfections and post-buckling patterns of the SMPC cylindrical shell under SPDI are insensitive to temperature (as shown in Figs. 4 and 11), and the same phenomenon was found in the MPDI method. Therefore, we do not distinguish the post-buckling patterns at different temperatures, and the post-buckling patterns at 25 °C are used as representatives in this section. The buckling loads and KDFs of the $[0/90/\pm45]_s$ SMPC cylindrical shell under different temperatures are calculated by the MPDI method, and the results are shown in Table 3. The buckling loads and KDFs obtained by the MPDI method are lower than those obtained by the SPDI method, but the variation tendency is similar: the buckling loads will decrease dramatically with increasing temperature, but the variation in the KDF is not obvious.

4.1.3. LBMI

To consider the geometric imperfections at different axial positions and better investigate the effect of temperature on the post-buckling patterns of the SMPC cylindrical shell, the LBMI method is also introduced. Different from the SPDI and MPDI techniques, the initial imperfection of the LBMI method is the 1st linear buckling mode of the cylindrical shell multiplied by a scaling factor δ, so we must study the convergence of δ. As shown in Fig. 14(a), the stiffness of the cylindrical shell can be significantly reduced by increasing the scaling factor δ. As δ increases from 0.05h to 0.3h (h is the thickness of the shell, which is 1.2 mm in this study), the buckling loads will gradually converge from 61.5 kN to 43.7 kN at room temperature. Therefore, δ is selected as 0.3h in the subsequent analysis.

Fig. 14(b) shows the variation in KDFs with temperature when δ = 0.3 h. The KDFs obtained by the LBMI method are lower than

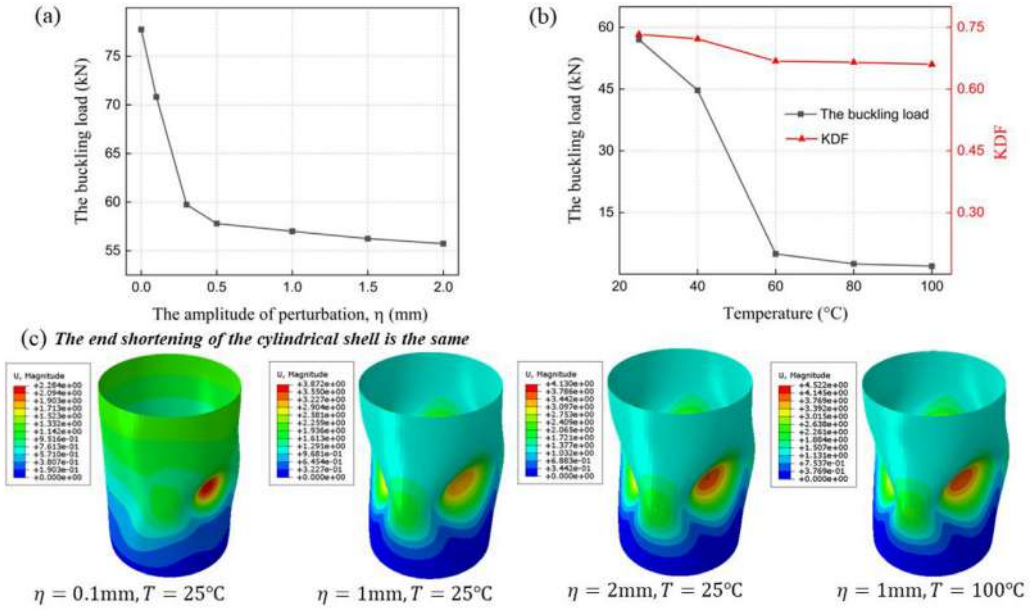

Fig. 11. The results of the SPDI method: (a) the variation in buckling loads with η at 25 °C, (b) the variations in buckling loads and KDFs with temperature when $\eta = 1$ mm, and (c) the post-buckling patterns of SMPC cylindrical shells.

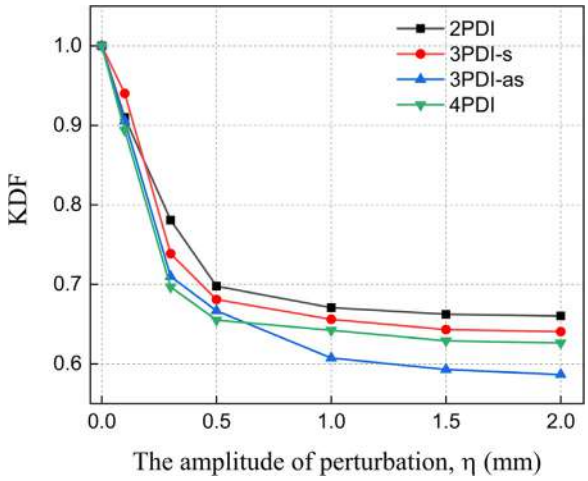

Fig. 12. The KDFs of the $[0/90/\pm45]_s$ SMPC cylindrical shell as a function of the perturbation displacements η at 25 °C.

those obtained by the SPDI and MPDI techniques, but the trend is similar. However, the post-buckling patterns of the SMPC cylindrical shell obtained by the LBMI method are sensitive to temperature, which will be quite different in low- and high-temperature regions. At the low-temperature region, the 1st linear buckling mode of the SMPC cylindrical shell is the regular spiral-shape deformation, so the post-buckling patterns of the LBMI method are dimple-shape deformations, which are similar to those of the SPDI and MPDI methods. At the high-temperature region, the 1st linear buckling mode shapes of the SMPC cylindrical shell distort, and irregular critical buckling modes are generated, so the post-buckling patterns transform from dimple-shape deformation into local folding-shape deformation. The initial imperfections and corresponding post-buckling patterns of the $[0/90/\pm45]_s$ SMPC cylindrical shell obtained by the SPDI, MPDI and LBMI methods are summarized in Fig. A.3. It should be noted that all the linear buckling modes of the SMPC cylindrical shell are distorted at high temperature, rather than not only the 1st modes, which can be seen in Fig. A.2. However, this phenomenon is not the focus of this study, and we will discuss this in detail in our future work.

4.2. Comparison of numerical and experimental results

The axial compressive load–displacement curves of $[0/90/\pm45]_s$ SMPC cylindrical shells at different temperatures are shown in Fig. 15. The load-bearing capacities of the SMPC cylindrical shell will decrease with increasing temperature. At 25 °C, the maximum load-bearing capacity of the SMPC cylindrical shell can exceed 30 kN. At a temperature of 100 °C, the cylindrical shell buckles when the axial compressive load is only 1.6 kN, thus losing part of the load-bearing capacity. In addition, the features of these curves are quite different in the low-temperature and high-temperature regions. As shown in Fig. 15(a) (at 25 °C and 40 °C), when the compressive force reaches a certain value, the compressive load–displacement curves will show a tendency of a leap downward, indicating that the cylindrical shell will be crushed, and the structure has entirely lost its load-bearing capacity. However, with the increase in temperature, as shown in Fig. 15(b), when the compressive force reaches the maximum value, it does not decline rapidly but slowly drops to a stable value. This indicates that the SMPC cylindrical shell will not be damaged at high temperatures, and the structure can still have a certain load-bearing capacity after buckling.

Table 4 shows the comparison of buckling loads from simulation and experimental results at different temperatures. At 25 °C and 40 °C, the numerical simulations greatly overestimate the load-bearing capacity of the SMPC cylindrical shell, and the deviation can reach 89%. When the temperature rises to 60 °C, 80 °C and 100 °C, the deviations will decrease gradually. The buckling loads obtained from the MPDI technique are in good agreement with the average values of the experimental results, where the error is less than 5%. The main reason for this phenomenon is that SMP is in its glassy state at low temperature (as seen from the DMA analysis), and the compressive strength of carbon fiber is much lower than its tensile strength. The compressive strain-to-failure of the SMPC is extremely low. Therefore, the SMPC cylindrical shell is more prone to undergoing compressive fracture than buckling deformation at relatively low temperatures, leading to its maximum load-bearing capacity being significantly lower than the simulation result. With increasing temperature, the SMP will gradually change from the glassy state to the rubbery state, and the SMPC can withstand large compressive and flexural deformations without fracture. Therefore, brittle fracture does not occur during the post-buckling deformation of the SMPC cylindrical shell; thus, the experimental results are in good agreement with the numerical results.

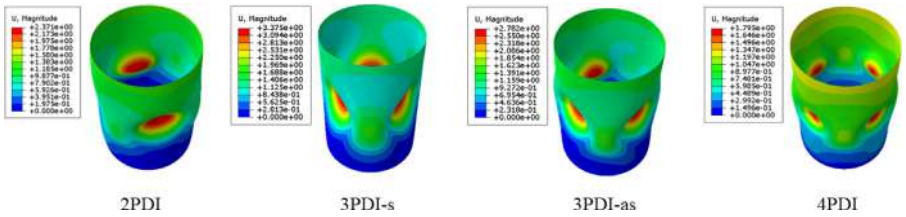

Fig. 13. The post-buckling pattern of $[0/90/\pm45]_s$ SMPC cylindrical shells with the same axial compressive displacement at 25 °C ($\eta = 1$ mm).

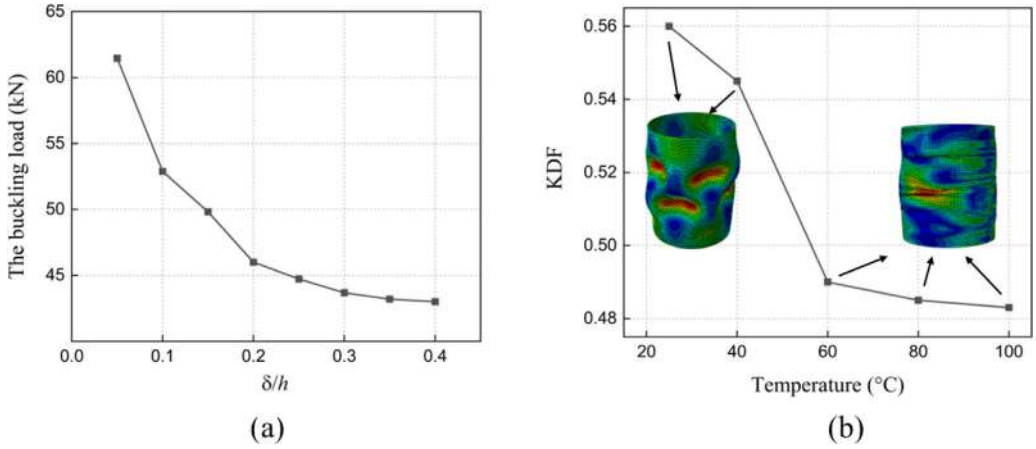

Fig. 14. The results of the LBMI method: (a) the variation in buckling loads with δ/h at 25 °C and (b) the variations in KDFs with temperature when $\delta = 0.3$ h.

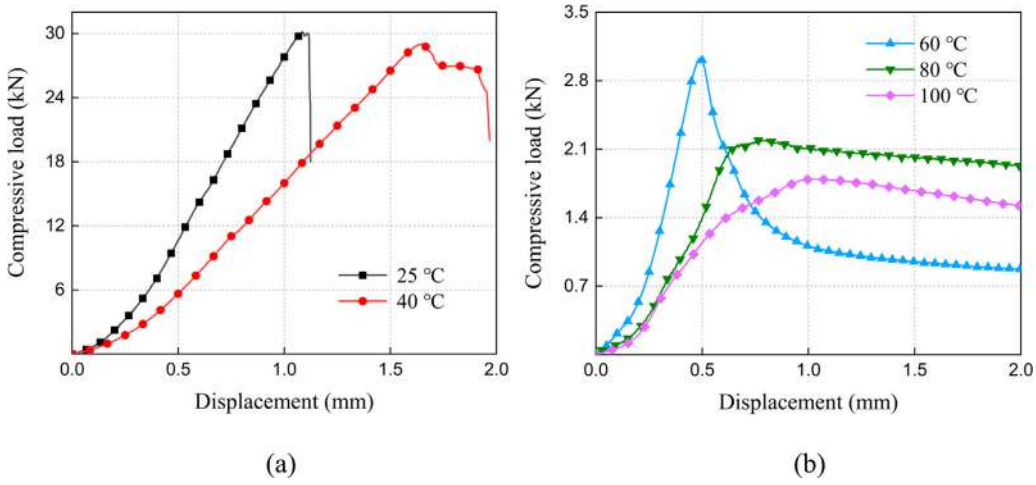

Fig. 15. The axial compressive load–displacement curves of $[0/90/\pm45]_s$ SMPC cylindrical shells at different temperatures: (a) low-temperature region and (b) high-temperature region.

Table 4
The buckling loads of $[0/90/\pm45]_s$ SMPC cylindrical shells from numerical simulations and experimental results at different temperatures, error = (FEA- Experiment)/ Experiment.

Temperature (°C)	Experimental bearing load (kN)	Buckling load by SPDI (kN)	*Error* (%)	Buckling load by 3PDI-as (kN)	*Error* (%)	Buckling load by LBMI (kN)	*Error* (%)
25	30.2 ± 1.4	57.0	*89.0*	47.2	*56.2*	44.7	*48.3*
40	29.0 ± 1622	44.7	*54.2*	38.3	*32.2*	35.7	*23.1*
60	3.03 ± 0.27	4.93	*62.7*	2.92	*−3.63*	2.60	*−14.2*
80	2.17 ± 0.15	2.52	*16.1*	2.13	*−1.70*	1.89	*−12.7*
100	1.67 ± 0.21	1.95	*17.0*	1.65	*−0.72*	1.47	*−11.7*

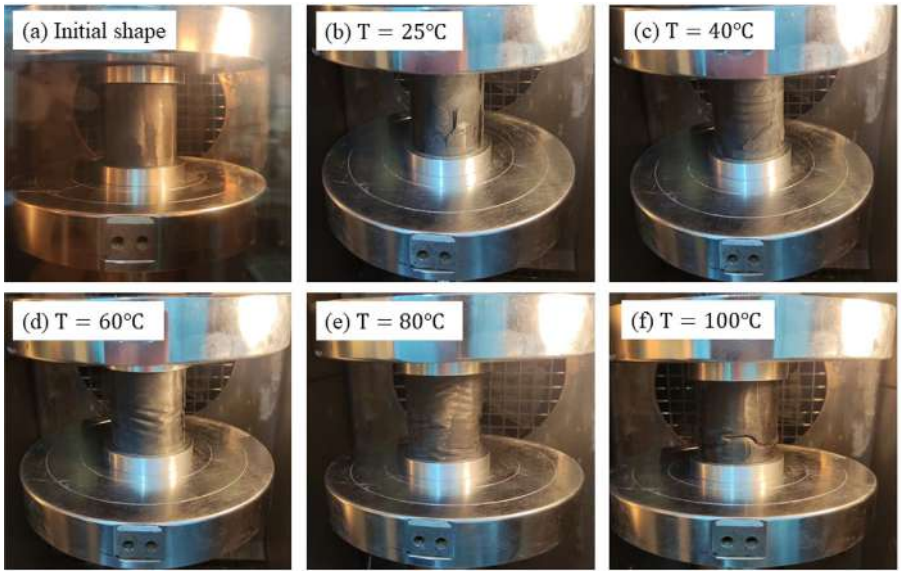

Fig. 16. The initial shape and deformation morphologies of SMPC cylindrical shells under axial compression at different temperatures.

Fig. 16 shows the initial shape and deformation morphology of SMPC cylindrical shells under axial compression at different temperatures with the same displacement. Fig. 16(b) and (c) show that at 25 °C and 40 °C, SMPC cylindrical shells are partially fractured, resulting in cracks and delamination damage, while the remaining parts do not undergo any deformation. This indicates that at low temperature, SMPC cylindrical shells are crushed instantaneously and lose their load-bearing capacity. However, at high temperatures, as shown in Fig. 16(d)–(f), SMPC cylindrical shells are not destroyed but undergo buckling deformation. The SMPC cylindrical shell buckles before being destroyed under the axial compressive load, and then the SMPC bears bending strain rather than compressive strain. As the temperature rises, the local bending strain also increases significantly, which will be very large when the temperature reaches 100 °C; however, no damage occurs, as shown in Fig. 16(f), and the structure can still have a certain load-bearing capacity, which is consistent with the analysis results above.

Fig. 17 shows the KDF of $[0/90/\pm45]_s$ SMPC cylindrical shells obtained from numerical simulations and experimental results at different temperatures. The KDFs calculated by the SPDI, MPDI and LBMI techniques decrease successively. In addition, in the low-temperature or high-temperature regions, the KDFs calculated by the same numerical method change little. Only when the temperature increases from 40 °C to 60 °C will the KDFs decrease by approximately 10%. In the low-temperature region, all the numerical methods overestimate the load-bearing capacity of the SMPC cylindrical shell, which is caused by the premature brittle fracture of SMPC. In the high-temperature region, the SPDI method overestimates the KDFs of the SMPC cylindrical shell, which is not safe in the preliminary design; the KDFs calculated by the MPDI are in good agreement with the average value of the experimental results, while in some test pieces, the experimental results are smaller than the simulation results, which may lead to a premature failure of the structure; the KDF calculated by the LBMI method is slightly smaller than the experimental results, with an error of approximately 10%, but it is safer than the MPDI method. In addition, it can be seen from Figs. 18 and A.3 that the post-buckling pattern of the SMPC cylindrical shell at high temperature obtained from the LBMI method is more consistent with the experimental result, while the SPDI and MPDI techniques cannot distinguish the influence of temperature on the post-buckling patterns.

In summary, in the preliminary design of SMPC cylindrical shells, numerical methods are not able to calculate the KDF at low temperatures well. Because the SMPC cylindrical shells are more prone to brittle fracture (rather than buckling deformation) at low temperature, the existing numerical methods are not able to distinguish them (brittle fracture and buckling) well. At high temperature, the LBMI method is an effective and safe method, and the corresponding post-buckling pattern is more consistent with the experimental result.

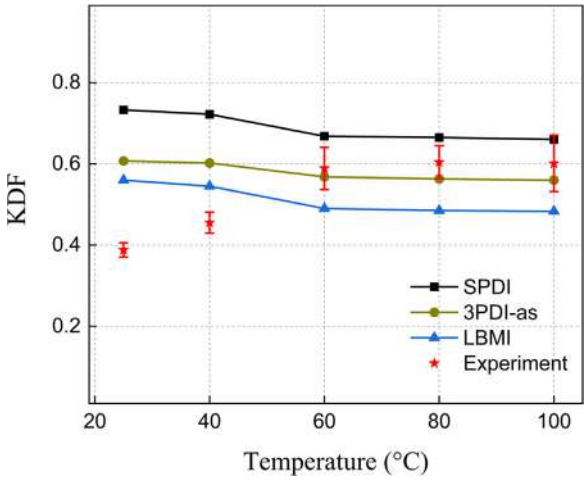

Fig. 17. The KDF of $[0/90/\pm45]_s$ SMPC cylindrical shells obtained from numerical simulations and experimental results at different temperatures.

5. The application assumption and repeatability experiments of buckled SMPC cylindrical shells

The abrupt unloading of prestress when the pyrotechnic releasing device explodes is one of the main causes of the instantaneous high impact of spacecraft. If the prestress can be released before the pyrotechnic releasing device explodes, the impact and noise can be effectively reduced. It can be seen in Section 4.2 that the SMPC cylindrical shell has an excellent axial load carrying capacity at low temperature, which can exceed 30 kN, and it is not prone to deform before being destroyed. While its buckling load will be greatly reduced at high temperature (1.67 kN), and large macroscopic compression deformation can occur without any damage. Using this characteristic, the SMPC cylindrical shell can be applied to the auxiliary vibration

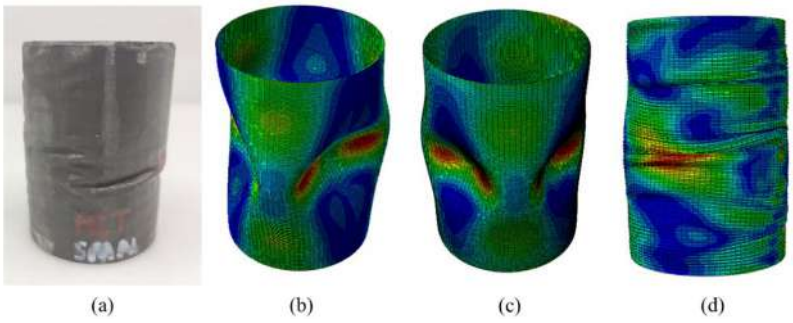

Fig. 18. The post-buckling patterns of $[0/90/\pm45]_s$ SMPC cylindrical shells in the high-temperature region with the same axial displacement determined by (a) experiment and (b) SPDI, (c) 3PDI-as, and (d) LBMI methods.

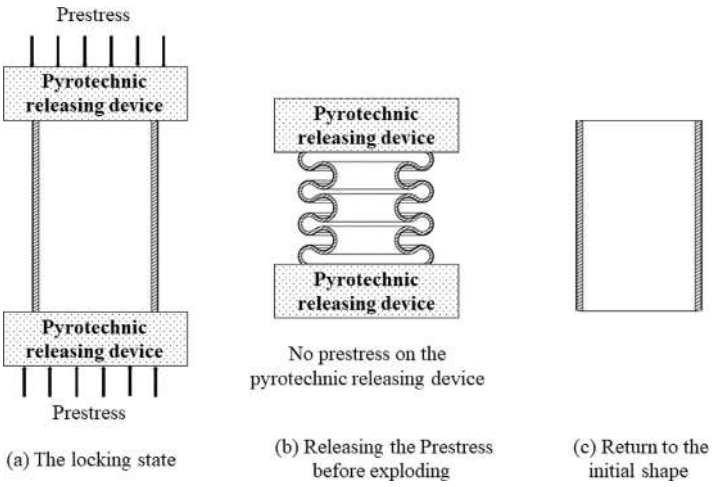

Fig. 19. The working process of the auxiliary vibration reduction structure of the space pyrotechnic releasing mechanism.

reduction structure of a space pyrotechnic releasing mechanism, which can avoid the disadvantages of an explosive impact and noise of existing pyrotechnic releasing devices. Its specific working process can be seen in Fig. 19 and is described as follows:

(a) The SMPC cylindrical shells should be installed in series with a conventional pyrotechnic releasing device. At the locking state, the SMPC cylindrical shell can effectively bear the prestress due to its characteristics of large load carrying capacity and small axial deformation before failure.

(b) Before the pyrotechnic releasing device explodes, the SMPC cylindrical shell needs to be heated. It will then buckle and shorten under the action of pre-compressive stress so that the prestress can be smoothly unloaded. When the pyrotechnic releasing device explodes, the instantaneous impact of the whole system at the small prestress state will be significantly reduced.

(c) After the SMPC cylindrical shell unloads the pre-compressive stress of the pyrotechnic releasing device, it can return to its initial shape after being reheated again to its T_g.

Fig. 20 shows that the SMPC cylindrical shell applied in this study can completely recover to its initial shape even after undergoing a large buckling deformation, which better reflects its shape memory capacity. Several repeated experiments were then carried out on the same SMPC cylindrical shell to measure its buckling load and deformation recovery ability. The results are shown in Fig. 21. This indicates that after 10 repeated "initial-buckled-recovery shape" cycles, the buckling load decreases from 1.67 kN to 1.49 kN, which is a decrease of only 10%, and in the last four cycles, it decreases by even less. Moreover, the SMPC cylindrical shell can return to its initial shape without any damage after 10 recovery cycles, so the repeatability of this kind of SMPC cylindrical shell is excellent.

6. Conclusion

In this study, axial compression experiments of $[0/90/\pm45]_s$ SMPC cylindrical shells at different temperatures are conducted. The SPDI, MPDI and LBMI techniques are used to investigate the effect of geometric imperfections on the buckling behaviors of SMPC cylindrical shells, and the corresponding buckling loads, KDFs and post-buckling patterns at different temperatures are compared with the experimental results. An auxiliary vibration reduction structure is proposed, and repeated experiments are carried out to verify the repeatability of the SMPC cylindrical shells. The main conclusions of this study are as follows:

(1) The buckling behaviors of SMPC cylindrical shells are very sensitive to temperature. In this study, the temperatures are divided into a low-temperature region and a high-temperature region, and the corresponding buckling behaviors at different temperature regions are investigated. In the low-temperature region, the SMPC cylindrical shell is more prone to brittle fracture than buckling deformation during the axial compressive experiment. In the high-temperature region, the SMPC cylindrical shell buckles before being destroyed.

(2) For the SPDI and MPDI techniques, the buckling loads and post-buckling patterns of SMPC cylindrical shells are closely related to the

Fig. 20. Shape-recovery process of the buckled SMPC cylindrical shell at 100 °C. (a) The post-buckling state and (b) the state after being reheated and recovering its shape.

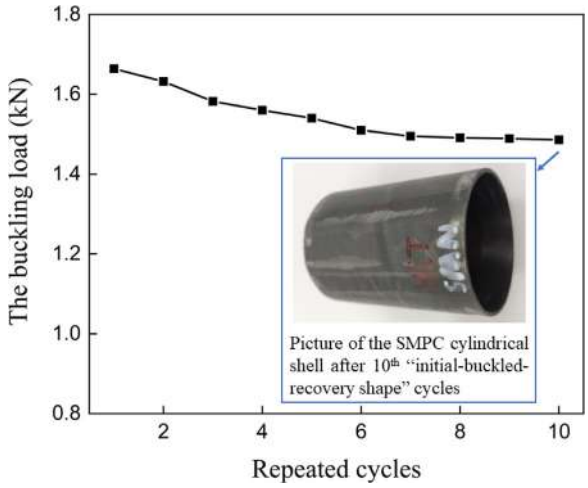

Fig. 21. The repeated "initial-buckled-recovery shape" experiment of an SMPC cylindrical shell at 100 °C.

number and amplitude of the perturbations, and the robust lower-bound buckling load can always be obtained when $\eta = 1$ mm. The KDFs obtained from the MPDI method are always lower than those of the SPDI method, and the increase in the number and degree of the asymmetric distribution of PDIs leads to a decrease in the KDF. Therefore, the 3PDI-as case is more sufficient to simulate the geometric imperfections of SMPC cylindrical shells.

(3) In the low-temperature region, all three imperfection methods overestimate the load-bearing capacity and KDF of the SMPC cylindrical shell because the existing numerical methods are not able to distinguish brittle fracture and buckling. In the high-temperature region, the SPDI method overestimates the KDFs; the KDFs calculated by the MPDI and LBMI techniques are in good agreement with the experimental results, while the LBMI method is safer and more conservative than the MPDI method in the preliminary design of SMPC cylindrical shells. In addition, only the LBMI method can distinguish the influence of temperature on the post-buckling patterns, and the corresponding post-buckling pattern is more consistent with the experiment.

(4) The buckling loads of the SMPC cylindrical shell obtained by numerical techniques are sensitive to temperature, while the KDFs are insensitive to temperature.

(5) The repeatability of the SMPC cylindrical shells is excellent at 100 °C. After 10 repeated "initial-buckled-recovery shape" cycles, the buckling loads only decrease by 10% and the shells do not show any irreversible damage.

CRediT authorship contribution statement

Hanxing Zhao: Writing – review & editing, Writing – original draft, Validation, Software, Methodology, Investigation, Formal analysis, Data curation. **Xin Lan:** Writing – review & editing, Visualization, Supervision, Project administration, Funding acquisition, Conceptualization. **Liwu Liu:** Validation, Supervision, Investigation, Conceptualization. **Yanju Liu:** Validation, Supervision, Resources, Project administration, Conceptualization. **Jinsong Leng:** Validation, Supervision, Resources, Project administration, Funding acquisition, Conceptualization.

Declaration of competing interest

The authors declare that they have no known competing financial interests or personal relationships that could have appeared to influence the work reported in this paper.

Data availability

Data will be made available on request.

Acknowledgments

The author would like to thank for the Heilongjiang Touyan Innovation Team Program. This work is supported by the National Natural Science Foundation of China (Grant No. 11632005, 11872020).

Appendix A

See Figs. A.1–A.3.

Appendix B. Supplementary data

Supplementary material related to this article can be found online at https://doi.org/10.1016/j.tws.2022.110340.

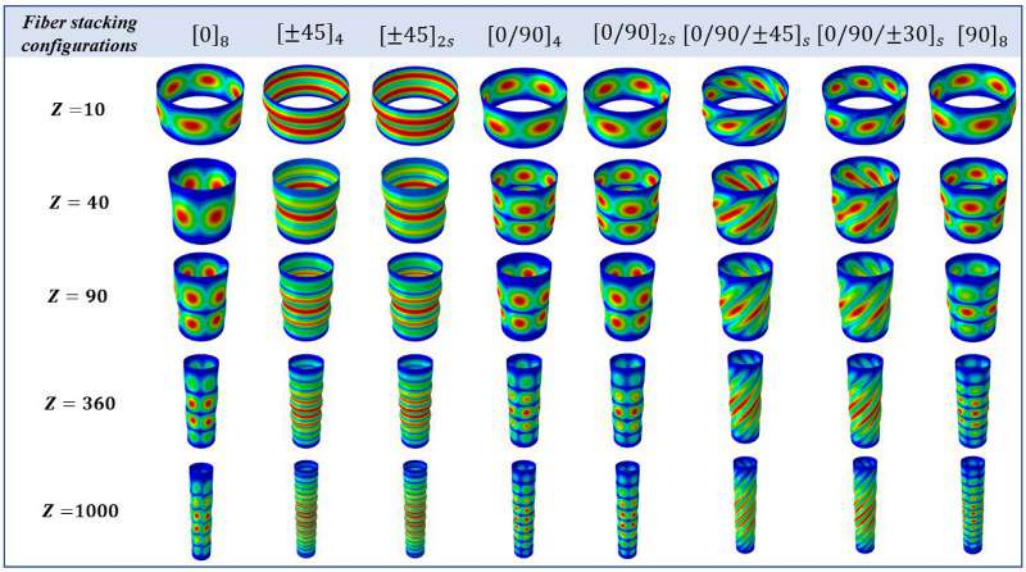

Fig. A.1. The 1st linear buckling mode shapes of SMPC cylindrical shells with different fiber stacking configurations and different values of the dimensional parameter Z at 25 °C (the deformation scale factor is 1).

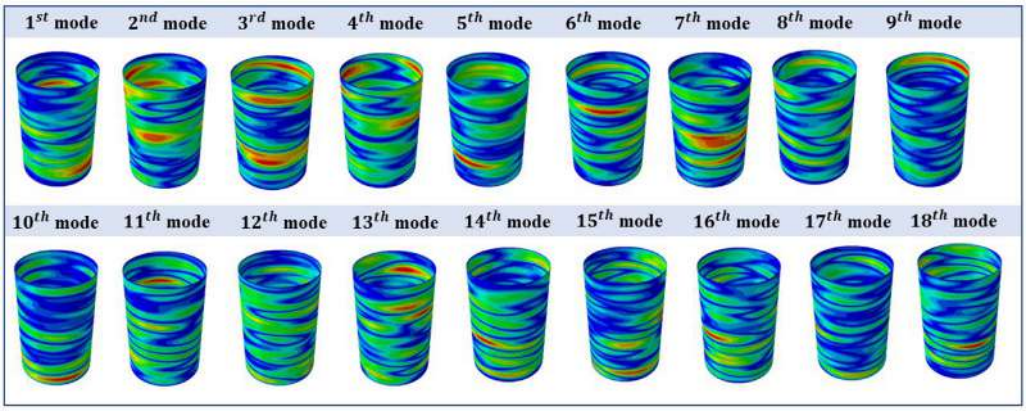

Fig. A.2. The linear buckling mode shapes of the $[0/90/\pm45]_s$ SMPC cylindrical shell at 100 °C (the deformation scale factor is 0).

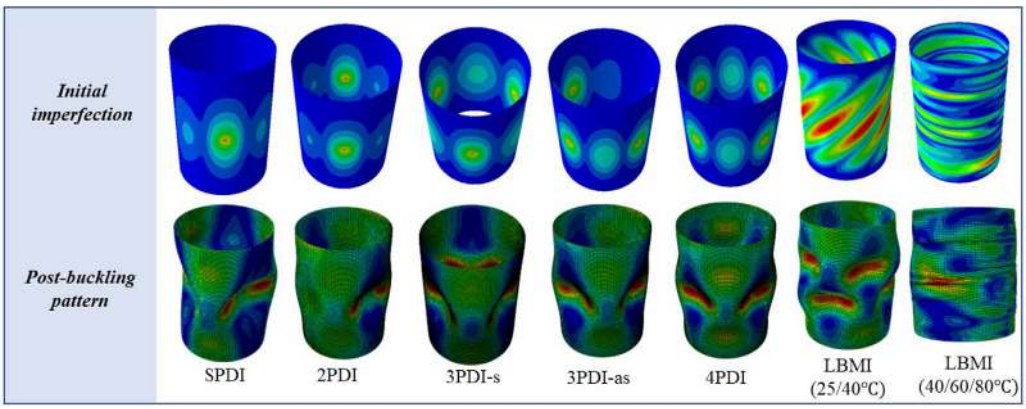

Fig. A.3. The initial imperfections and corresponding post-buckling pattern (Mises-stress contours) of SMPC cylindrical shells by numerical simulations.

References

[1] N. Li, P. Chen, X. Ling, A microscopic elasto-plastic damage model for characterizing transverse responses of unidirectional fiber-reinforced polymer composites, Thin Wall Struct. 154 (2020) 106828.

[2] H. Ye, X. Zhou, J. Ma, H. Wang, Z. You, Axial crushing behaviors of composite pre-folded tubes made of KFRP/CFRP hybrid laminates, Thin Wall Struct. 149 (2020) 106649.

[3] J. Jang, S. Hong, J. Kim, et al., Accelerated testing method for predicting long-term properties of carbon fiber-reinforced shape memory polymer composites in a low earth orbit environment, Polymers 13 (10) (2021) 1628.

[4] T.D. Dao, N.S. Goo, W.R. Yu, Blocking force measurement of shape memory polymer composite hinges for space deployable structures, J. Intell. Mater. Syst.

Struct. 29 (18) (2018) 1045389X1879895.
[5] Y. Xia, Y. He, F. Zhang, et al., A review of shape memory polymers and composites: mechanisms, materials, and applications, Adv. Mater. 33 (6) (2020) 2000713.
[6] Y. Liu, H. Du, L. Liu, et al., Shape memory polymers and their composites in aerospace applications: a review, Smart Mater. Struct. 23 (2014) 023001.
[7] C. Tian, R. Osama, L. Robert, et al., Autonomous deployment of a solar panel using elastic origami and distributed shape-memory-polymer actuators, Phys. Rev. Appl. 11 (6) (2019) 064069.
[8] Z. Ren, Y. Sun, Q. Li, et al., Manufacture and investigation on the shape memory polymer composite subsidy pipe, Compos. Struct. 274 (2021) 114331.
[9] H. Du, L. Liu, F. Zhan, et al., Thermal-mechanical behavior of styrene-based shape memory polymer tubes, Polym. Test 57 (2017) 119–125.
[10] T. Fathollah, O. Milad, Buckling of axially compressed composite cylinders with geometric imperfections, Steel Compos. Struct. 29 (2018) 557–567.
[11] H. Wagner, C. Huhne, S. Niemann, et al., Robust knockdown factors for the design of cylindrical shells under axial compression: Analysis and modeling of stiffened and unstiffened cylinders, Thin Wall Struct. 127 (2018) 629–645.
[12] T. Fathollah, A. Ramadan, T. Farid, Response of perforated composite tubes subjected to axial compressive loading, Thin Wall Struct. 50 (2012) 174–181.
[13] B. Wang, P. Hao, X. Ma, K. Tian, Knockdown factor of buckling load for axially compressed cylindrical shells: state of the art and new perspectives, Acta Mech. Sin. Proc. 38 (2022) 421440.
[14] L. Friedrich, T.A. Schmid-Fuertes, K.U. Schroder, Comparison of theoretical approaches to account for geometrical imperfections of unstiffened isotropic thin-walled cylindrical shell structures under axial compression, Thin Wall Struct. 92 (2015) 1–9.
[15] C. Huhne, R. Rolfes, E. Breitbach, et al., Robust design of composite cylindrical shells under axial compression-simulation and validation, Thin Wall Struct. 46 (7) (2008) 947–962.
[16] V.I. Weingarten, P. Seide, J.P. Peterson, NASA SP-8007-buckling of thin-walled circular cylinders. NASA Space Veh. Des. Criter Struct 1965 (revised 1968). Local buckling.
[17] B. Wang, K. Du, P. Hao, et al., Numerically and experimentally predicted knockdown factors for stiffened shells under axial compression, Thin Wall Struct. 109 (2016) 13–24.
[18] B. Wang, S. Zhu, P. P. Hao, et al., Buckling of quasi-perfect cylindrical shell under axial compression: a combined experimental and numerical investigation, Int. J. Solids Struct. 130 (2018) 232–247.
[19] E.M. Sosa, L.A. Godoy, J. Croll, Computation of lower-bound elastic buckling loads using general-purpose finite element codes, Compos. Struct. 84 (2006) 1934–1945.
[20] I. Elishakoff, B. Kriegesmann, R. Rolfes, C. Huhne, A. Kling, Optimization and ant-optimization of buckling load for composite cylindrical shells under uncertainties, AIAA J. 50 (7) (2012) 1513–1524.
[21] M. Arbelo, R. Degenhardt, et al., Numerical characterization of imperfection sensitive composite structures, Compos. Struct. 108 (2014) 295–303.
[22] P. Jiao, Z. Chen, X. Tang, et al., Design of axially loaded isotropic cylindrical shells using multiple perturbation load approach – simulation and validation, Thin Wall Struct. 133 (2018) 1–16.
[23] D. Zhang, Z. Chen, Y. Li, et al., Lower-bound axial buckling load prediction for isotropic cylindrical shells using probabilistic random perturbation load approach, Thin Wall Struct. 155 (2020) 106925.
[24] N. Wagner, C. Hühne, et al., Stimulating the realistic worst case buckling scenario of axially compressed unstiffened cylindrical composite shells, Compos. Struct. 160 (2017) 1095–1104.
[25] S. Abolfazl, T. Fathollah, O. Milad, Orientation and size effect of a rectangle cutout on the buckling of composite cylinders, Aerosp. Sci. Technol. 87 (2019) 488–497.
[26] T. Fathollah, O. Milad, M. Shokrieh, Experimental and numerical investigation of buckling behavior of composite cylinders with cutout, Thin Wall Struct. 116 (2017) 136–144.
[27] A. Evkin, Analytical model of local buckling of axially compressed cylindrical shells, Thin Wall Struct. 168 (2021) 118261.
[28] A. Evkin, V. Krasovsky, et al., Local buckling of axially compressed cylindrical shells with different boundary conditions, Thin Wall Struct. 141 (2019) 374–388.
[29] J. Horak, G. Lord, M. Peletier, Cylindrical buckling: The mountain pass as an organizing center, SIAM J. Appl. Math. 6 (2006) 1793–1824.
[30] A. Evkin, Local buckling of cylindrical shells. Pogorelov's geometrical method, in: Problems of Nonlinear Mechanics, Springer, 2018, pp. 369–391.
[31] E. Sosa, L. Godoy, J. Croll, Computation of lower-bound elastic buckling loads using general-purpose finite element codes, Comput. Struct. 84 (2016) 1934–1945.
[32] X. Ma, P. Hao, F. Wang, B. Wang, Incomplete reduced stiffness method for imperfection sensitivity of cylindrical shells, Thin Wall Struct. 157 (2021) 107148.
[33] P. Jiao, Z. Chen, H. Ma, et al., Buckling behaviors of thin-walled cylindrical shells under localized axial compression loads, part 1: Experimental study, Thin Wall Struct. 166 (2021) 108118.
[34] P. Jiao, Z. Chen, H. Ma, et al., Buckling behaviors of thin-walled cylindrical shells under localized axial compression loads, part 2: Numerical study, Thin Wall Struct. 169 (2021) 108330.
[35] P. Jiao, Z. Chen, F. Xu, et al., Effects of ringed stiffener on the buckling behavior of cylindrical shells with cutout under axial compression: Experimental and numerical investigation, Thin Wall Struct. 123 (2018) 232–243.
[36] P. Jiao, Z. Chen, H. Ma, A new design method for axially loaded thin-walled cylindrical shells based on elasto-plastic buckling analysis, ASEM PVP 3 (2019) 154932.
[37] F. Li, Fabrizio Scarpa, X. Lan, Y. Liu, J. Leng, Bending shape recovery of unidirectional carbon fiber reinforced epoxy-based shape memory polymer composites, Composites A 116 (2019) 169–179.